JGR Oceans

Fate of Internal Waves on a Shallow Shelf

Kristen A. Davis[1] [ID], **Robert S. Arthur[2]** [ID], **Emma C. Reid[1]** [ID], **Justin S. Rogers[3]** [ID], **Oliver B. Fringer[3]**, **Thomas M. DeCarlo[4]** [ID], **and Anne L. Cohen[5]** [ID]

[1]Department of Civil and Environmental Engineering and Earth System Science, University of California, Irvine, Irvine, CA, USA, [2]Lawrence Livermore National Laboratory, Livermore, CA, USA, [3]Department of Civil and Environmental Engineering, Stanford University, Stanford, CA, USA, [4]Massachusetts Institute of Technology/Woods Hole Oceanographic Institution Joint Program in Oceanography and Applied Ocean Science and Engineering, Cambridge, MA, USA, [5]Department of Geology and Geophysics, Woods Hole Oceanographic Institution, Woods Hole, MA, USA

Abstract Internal waves strongly influence the physical and chemical environment of coastal ecosystems worldwide. We report novel observations from a distributed temperature sensing (DTS) system that tracked the transformation of internal waves from the shelf break to the surf zone over a narrow shelf slope region in the South China Sea. The spatially continuous view of temperature fields provides a perspective of physical processes commonly available only in laboratory settings or numerical models, including internal wave reflection off a natural slope, shoreward transport of dense fluid within trapped cores, and observations of internal rundown (near-bed, offshore-directed jets of water preceding a breaking internal wave). Analysis shows that the fate of internal waves on this shelf—whether transmitted into shallow waters or reflected back offshore—is mediated by local water column density structure and background currents set by the previous shoaling internal waves, highlighting the importance of wave-wave interactions in nearshore internal wave dynamics.

1. Introduction

Internal waves propagate in the stratified waters of the subsurface ocean and are ubiquitous and well-studied features of continental shelves (Garrett & Munk, 1979; Helfrich & Melville, 2006). Large-amplitude internal waves interact with shoaling bathymetry and can break, run up, and form bottom-propagating, bore-like features on the shelf as far inshore as the surfzone (Boegman et al., 2005b in lakes; Klymak & Moum, 2003; MacKinnon & Gregg, 2003; McSweeney et al., 2020; Sinnett & Feddersen, 2014; Sinnett et al., 2018; Walter et al., 2012; Walter et al., 2014; Winant, 1974). Internal wave dynamics have important implications for vertical mixing, cross-shelf transport, environmental variability, and the exchange of heat, nutrients, sediments, larvae, and pollutants in coastal ecosystems globally (Cheriton et al., 2014; Davis & Monismith, 2011; Emery & Gunnerson, 1973; Henderson, 2016 in lakes; Hofmann et al., 2011; Leichter et al., 1996; Lucas et al., 2011; Omand et al., 2011; Pineda, 1991; Wolanski & Pickard, 1983).

Currently, the most comprehensive picture of internal wave dynamics on the shelf, including breaking, the distribution of energy, and mixing, comes from laboratory and numerical studies (Arthur et al., 2017; Arthur & Fringer, 2014; Helfrich, 1992; Lamb & Nguyen, 2009; Michallet & Ivey, 1999; Venayagamoorthy & Fringer, 2007). Field observations of shoaling internal waves are challenging due to the wide variability of waveforms and spatiotemporal scales that characterize associated processes such as breaking and dissipation. Despite these challenges, existing observations demonstrate that internal waves on the continental slope and shelf often occur as steepened internal tides (Martini et al., 2013; Scotti et al., 2007) or remotely generated internal solitary waves (ISWs) (Li & Farmer, 2011; Zhao et al., 2014). ISWs are nonlinear dispersive waves that propagate as waves of depression or elevation, where the displacement of isopycnals is downward or upward, respectively, depending upon the stratification. As ISWs of depression move into shallower water near the coast, they can change polarity into waves of elevation or fission into trains of smaller ISWs (Lamb, 2014; Orr & Mignerey, 2003). On the inner shelf, large-amplitude internal waves generally evolve into bottom-propagating internal bores or boluses (Davis & Monismith, 2011; Pineda, 1999; Sinnett et al., 2018; Walter et al., 2012; Walter et al., 2017). An internal bore is essentially an upslope-propagating hydraulic jump that has a shock-like front, or "head" followed by a dense (cold) "tail" of fluid. An

internal bolus, observed as a discrete mass of dense fluid without a long tail, is an ISW of elevation with a trapped core of dense fluid (Bourgault et al., 2007; Bourgault et al., 2008; Lamb, 2014). However, the lines blur between these waveform classifications, and it is not uncommon to see internal motions with both wave-like and bore-like characteristics on the shelf, that is, "solibores" (Henyey & Hoering, 1997; Hosegood et al., 2004). What is clear is that the inner shelf is a region of complex internal wave interaction with topography, rapidly changing stratification and background currents, and that the fate of these waves is important for nearshore ecosystems (Green et al., 2018; Reid et al., 2019; Wall et al., 2015; Walter et al., 2014).

In this paper, we present observations of internal waves shoaling on the shallow shelf slope of Dongsha Atoll, a coral reef ecosystem in the South China Sea (Figures 1a–1c). Dongsha is directly in the path of some of the world's largest ISWs (Alford et al., 2015; Guo & Chen, 2014; Hsu & Liu, 2000; Lien et al., 2005). These waves evolve from steepened internal tides in the Luzon Strait and propagate westward across the deep basin of the northern South China Sea with wavelengths of $O(3–10$ km), often developing into wave trains (Alford et al., 2015). As the solitary waves shoal up onto the continental slope, they steepen even further with amplitudes as large as 150–200 m and wavelengths of only a few hundred meters. At this point, they can become susceptible to both convective and shear instabilities which cause them to break and drive huge vertical overturns, energetic mixing, and energy dissipation (Chang et al., 2006; St. Laurent, 2008).

The shallow (<25 m) slope of Dongsha Atoll is an internal swash zone, where the end of life of these large internal waves takes the form of bottom-propagating solibores and boluses. They spend their remaining energy bringing deep water up to the surface where it has significant effects on the reef heat and nutrient budgets (Reid et al., 2019). From 1–17 June 2014, we deployed Distributed Temperature Sensing (DTS) instrumentation to capture spatially continuous observations of near-bed temperature on the fore reef slope of Dongsha Atoll to evaluate the path (or "fate") of internal waves shoaling onto the shelf and moorings to measure the vertical structure of velocity and density stratification. A semi-idealized numerical simulation is used to help interpret the novel perspective provided by the DTS observations. Our results are among the first reported DTS deployments in the coastal ocean (but see also Connolly & Kirincich, 2018; Reid et al., 2019) and enable a continuous view of internal wave evolution across a narrow, steep shelf and the resulting benthic temperature environment.

2. Methods

2.1. Site Description

Dongsha Atoll is 28 km in diameter and has an area of approximately 600 km^2. The atoll sits at the eastern edge of the continental shelf, also known as the Dongsha Plateau (Figure 1a). Our study site is located on the eastern side of the island where the bathymetric slope is fairly steep. The fore reef has a 0.03–0.05 slope down to 25-m depth, where a steeper 0.15 slope section extends to a depth of 50 m, after which the slope flattens slightly (0.07) down to 300-m depth. The "shelf" on the eastern side of Dongsha Atoll is therefore very narrow, but here we will define the inner shelf to be shoreward of the 25-m isobath. This definition of the inner shelf reflects a topographic division (slope change) and is also the location where the time-averaged thermocline depth intersects the bed.

The east reef flat (inshore of the slope) is roughly 3 km wide and ranges from 0.6- to 3.5-m depth. A survey of the benthic composition of the reef flat shows that the region is dominated by fleshy algae, sea grass, and live coral (DeCarlo et al., 2017). The reef slope has well-developed spur and groove formations, dominated by Scleractinia (stony corals) and Octocorallia (soft corals).

General ocean circulation in the northern South China Sea during the summer is controlled by monsoon winds (Song, 2011). Winds from the southwest drive surface currents generally to the northeast (Morton & Blackmore, 2001). The barotropic (surface) tide at Dongsha Atoll is mixed semidiurnal, and barotropic tidal currents are oriented primarily alongshore, with amplitudes of up to 0.5 ms^{-1}.

2.2. DTS Observations

Fiber optic (FO) DTS relies on the relation between the thermal energy state of an optical fiber and Raman backscatter intensities. Light is backscattered as a coherent pulse of light from a laser propagates through the fiber. Within the spectrum of the backscattered light, the Raman frequency bands (known as the Stokes and anti-Stokes peaks) are influenced by the thermal energy state of the scattering site. The ratio of the
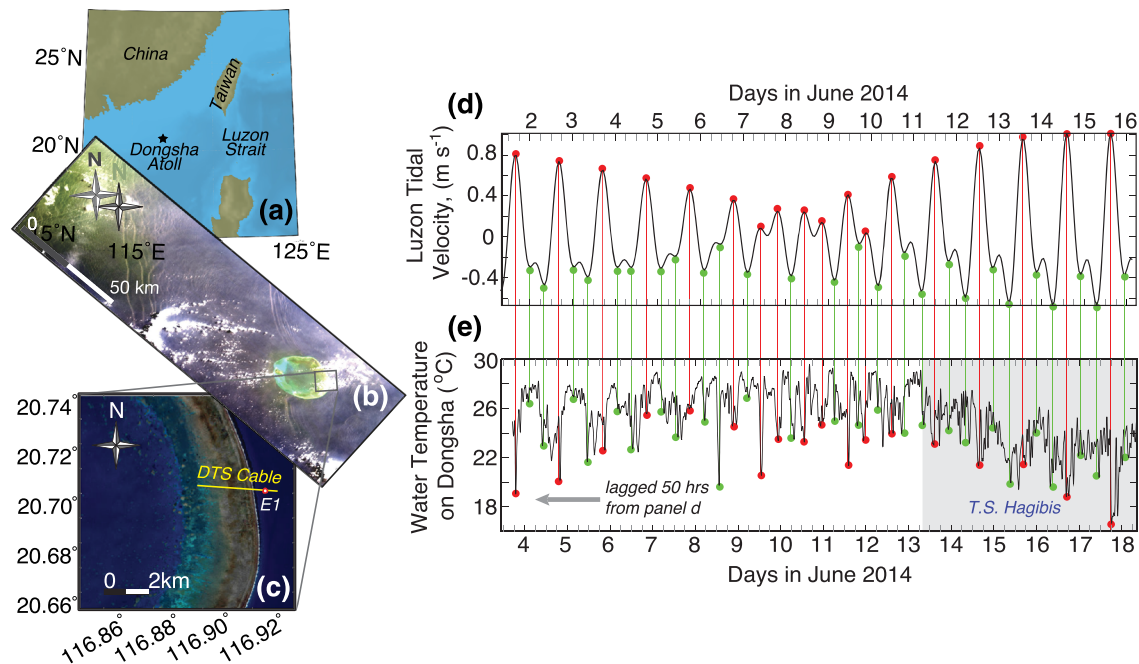
Figure 1. South China Sea internal waves. (a) Map of northern South China Sea indicating experiment location on Dongsha Atoll. (b) Internal waves refracting around Dongsha Atoll in a Hyperspectral Image for the Coastal Ocean (HICO) taken on 28 May 2014. (c) Image of Dongsha Atoll eastern reef from the Taiwan National Space Organization with location of DTS fiber optic cable and Mooring E1. (d) Depth-averaged, eastern component of tidal velocity in the Luzon Strait (20.6°N, 121.9°E). (e) 1-h low-pass filtered near-bed water temperature at Mooring E1 on the Dongsha Atoll fore reef, lagged 50 h behind the tidal velocities in (d). Vertical lines between panels (d) and (e) are to aid in visual alignment of tidal flow maxima (red is ebb, green is flood) and temperature on Dongsha fore reef. Time is in local time (GMT+8). Tropical storm Hagibis arrived near Dongsha Atoll near the end of the study period.

anti-Stokes to Stokes signal is exponentially dependent upon the temperature of the fiber at the scattering site (Tyler et al., 2009). The distance along the cable is determined from the time of flight of the light through the fiber. Combining the temperature measurement from the Raman spectra with the distance measurement allows the DTS to measure a profile of temperature along the length of the optical fiber.

The precision of the DTS temperature measurement is a function of the total number of photons detected to constrain the anti-Stokes/Stokes ratio. Thus, there are trade-offs between temperature measurement precision and spatial or temporal resolution—the higher the spatial or temporal resolution, the fewer photons observed per measurement (Hausner et al., 2011). Additionally, the strength of the optical signal decays with distance from the source, so sections of the cable farther from the DTS instrument require longer integration times to achieve a desired level of precision. The FO cable is assumed to be in thermal equilibrium with the surrounding fluid. For a more detailed review of the DTS theory, the reader is referred to several publications on the topic (Hausner et al., 2011; Rogers, 1999; Tyler et al., 2009; Vercauteren et al., 2011). DTS systems have been deployed in a number of other environments to measure temperatures at spatial scales from meters to kilometers (Hausner et al., 2011; Hilgersom et al., 2016; Kobs et al., 2014; Selker et al., 2006; Suárez et al., 2011; Tyler et al., 2009; van Emmerik et al., 2013; Vercauteren et al., 2011).

The optimal use of the DTS instrument in coastal ocean environments is where a strong temperature gradient intersects the bed. This is true for our field site at Dongsha Atoll, where the large-amplitude ISWs have broken offshore and are running up along the bed as bottom-propagating solibores and boluses. On the Dongsha fore reef slope, temperature differences across the thermal front at the leading edge of the internal solibores are typically >2 °C and can be up to 10 °C. Here a four-channel DTS system (Sensornet Oryx) was used to capture a continuous view of near-bed temperature in a cross-shelf profile on the east fore reef of Dongsha Atoll. Four kilometers of Kaiphone, a 0.6-cm diameter FO cable was deployed in a cross-shelf orientation (285°, aligned approximately parallel to the propagation direction of the offshore internal wave field (Ramp et al., 2010)), beginning at the back of the reef flat (~2-m depth) and terminating offshore at 50-m depth on the fore reef (Figure 1c). In this study, we focus on the offshore-most ~1 km of the FO

cable—from the reef crest down the fore reef slope. The reader is referred to Reid et al. (2019) for further information about the shallow reef DTS results. The FO cable followed the bottom contours of the bed, except in areas with extreme changes in topography (such as a coral groove) where the cable was raised above the bed by up to 0.5 m. The DTS collected temperature traces along the cable every minute with 2-m spatial resolution from 2–12 June 2014. A tropical storm in the vicinity of Dongsha Atoll reduced solar power and prevented further DTS measurements after 12 June; however, measurements from vertical arrays (section 2.3) continued until 17 June 2014.

One limitation of the linear, cross-shore configuration of our cable deployment is that it was not able to resolve the alongshore component of the internal wave phase speed. However, the relatively singular source of the internal waves shoaling on the Dongsha Atoll fore reef (Luzon Strait, discussed further in section 3.1) and the alignment of the cable with the well-constrained direction of propagation of the biggest internal waves in the northern South China Sea (Ramp et al., 2010) give us confidence that the waves are propagating in approximately the same direction as the cable. For example, observations by Ramp et al. (2010) of ISW propagation in the northern South China Sea collected over 15 months demonstrate that the waves travel WNW towards 282°–288° with little variation (i.e., within ~3° of parallel to the FO cable). Additionally, we assume that the waves have largely refracted to the local bathymetry in depths shallower than 50 m. Furthermore, even with a 20° angle between the direction of internal wave propagation and the FO cable line, the apparent phase speed would only be 6% greater than the true phase speed.

After deployment, scuba divers surveyed the FO cable above 30-m depth, collecting location and depth data associated with specific meter markings on the cable. For optimal DTS calibration, it is necessary to maintain known temperature reference sections at a range of different temperatures along the FO cable for the entire deployment (Hausner et al., 2011). In this study, the FO cable was configured with four 20-m coiled reference sections, each with a known temperature from a colocated, independently logging, temperature sensor (Seabird SBE-56, accuracy 0.002 °C). One reference section was kept in a recirculating ice bath on a scaffolding platform. Calibration parameters relating the Raman backscatter intensity to the optical fiber temperature are derived from independent accurate temperature measurements in the reference sections following the methods of Hausner et al. (2011). In addition to the temperature loggers used for calibration, several point temperature sensors were deployed along the cable length for validation purposes. Validation of the DTS temperature against independent temperature sensors (SBE-56s) gives an average root mean square error (RMSE) = 0.20 °C and a bias of 0.07 °C.

The spatially continuous temperature data from the DTS instrument allow for the calculation of the exact nonlinear wave characteristics. Wave characteristic lines were estimated from thermal fronts in the DTS data that were manually digitized (see e.g., Figure 5b). The phase speed of the internal waves was estimated from the wave characteristic lines as $c_{ph} = dx/dt$, where dx is the change in cross-shore distance and dt is the change in time.

2.3. Additional Physical Oceanographic Measurements

In addition to the DTS system, currents and vertical water column structure were measured from 3–17 June 2014 at Mooring E1 (Figure 1c). One upward-looking acoustic wave and current profiler (AWAC, Nortek AS) was deployed at 18-m depth near the FO cable and recorded current measurements at 1-min intervals. Just downslope, at 24-m depth, a vertical array of thermistors (Seabird Electronics SBE-56s, sampled at 2 Hz) was deployed with 2-m vertical spacing (between 2.8 and 16.8 m above the bed) with a conductivity–temperature–depth (CTD) sensor (SBE-37, sampled once per minute) 1.2 m above the bed.

Tidal velocities in Luzon Strait were estimated using the Oregon State Tidal Inversion Software (OTIS; Egbert & Erofeeva, 2002) and the TMD toolbox (Padman & Erofeeva, 2004). Background stratification, or Brunt Väisälä buoyancy frequency, was calculated as $N^2 = -(g/\rho_0)\rho_z$, where g is gravitational acceleration, ρ_0 is a reference density, and ρ_z is the vertical gradient in density. Density was calculated from 1 h averaged temperature and conductivity data compiled from the vertical array of temperature sensors at E1 and below 25 m from the DTS FO cable.

Apparent internal wave phase speeds measured by the DTS are compared with the phase speed of a long linear, first-mode internal wave in a stratified fluid, estimated as

$$c_{ph(linear)} = \frac{H}{\pi} \left(N^2 - \omega^2 \right)^{1/2}, \tag{1}$$

where H is water depth, N^2 is averaged over depth and time for the entire deployment period, and ω is the angular frequency of the wave (Kundu & Cohen, 2002; Venayagamoorthy & Fringer, 2007).

2.4. Nitrate Measurements

Water samples were collected at depths from 2–10 m, every 2 or 3 h on 4–5 June 2014 from the R/V Ocean Researcher III anchored near Mooring E1 and in surface waters around Dongsha Atoll (<40-m depth) in October 2012 (Wong et al., 2015). Water was collected using a Go-Flo bottle, and nitrate concentrations were determined according to the methods of Parsons et al. (1984) . A linear fit between nitrate concentrations and water temperature ($R^2 = 0.74$, $p < 0.001$) was used to estimate nitrate concentration from DTS temperature (further details and data shown in Reid et al., 2019). Note that while this simple relationship is useful for estimating nutrient concentrations on the fore reef (very near to the sample collection site), it does not account for biological transformations of the nutrient fields, such as uptake or remineralization.

2.5. Numerical Simulations

Despite the complexity of the realistic internal wave field, semi-idealized, two-dimensional numerical simulations can be used to improve understanding of field observations of breaking internal waves on slopes (Bourgault et al., 2007; Walter et al., 2012). Here, a semi-idealized numerical model is used to complement the DTS observations and to explore how the internal wave structure and dynamics over the entire water column might lead to the observed patterns in the DTS temperature data. The nonlinear, nonhydrostatic model SUNTANS (Fringer et al., 2006) is employed along a two-dimensional cross section that extends eastward offshore of Dongsha Atoll along 20.7°N (bathymetry from field surveys and Wang et al., 2007). The cross section used in the model approximately follows that of the FO cable (noting that the cable is not oriented exactly east–west near the atoll, but the differences in orientation between the observations and model domain are considered negligible) and extends farther offshore (reaching a depth of 300 m), where a 5-km flat section is added to allow for wave initialization. The model has a horizontal grid spacing dx = 3 m, a vertical grid spacing dz = 3 m, a vertical grid with 100 z-level cells, 3% stretching, and vertical spacing dz = 9.01 m at depth which decreases to 0.50 m near the surface for increased resolution, and a time step dt = 0.5 s. This value of dx meets the grid lepticity requirement of Vitousek and Fringer (2011) for resolving nonhydrostatic effects, which are important in shoaling and breaking internal waves. A drag coefficient $C_d = 0.005$ is used with a quadratic drag law formulation for the velocity boundary condition on the bottom, while a free slip condition is used on the nearshore and offshore walls. The density boundary conditions are gradient free on all walls. A constant eddy diffusivity of $\nu = 10^{-4}$ m^2/s is used.

SUNTANS simulations were initialized with a smoothed vertical profile of salinity and temperature from CTD measurements taken just offshore of the east Dongsha fore reef during a hydrographic cruise by the R/V Ocean Researcher III on 6 June 2014. A solitary-like wave structure was initialized in the offshore flat part of the domain using a two-dimensional mathematical model of the fully nonlinear, inviscid, steady-state Dubriel-Jacotin-Long (DJL) equation with background current. The DJL model, as given by Stastna and Lamb (2002), is

$$\nabla^2 \eta + \frac{U'(z-\eta)}{c - U(z-\eta)} \left[\eta_x^2 + (\eta_z - 2)\eta_z \right] + \frac{N^2(z-\eta)}{[c - U(z-\eta)]^2} \eta = 0, \tag{2}$$

where $\eta(x,z)$ is the isopycnal displacement, c is the internal wave phase speed, $U(z)$ is the background current (assumed zero for this study), and $N(z)$ is the background Brunt Väisälä buoyancy frequency. Mode-one solutions to this equation are found iteratively using the DJL equation solver (DJLES) MATLAB package (Dunphy et al., 2011; Turkington et al., 1991) and the depth-integrated available potential energy (APE = 18.8 MJ/m) measured by Fu et al. (2012) at a site located at 285-m depth on the slope, with an initial maximum isopycnal displacement of approximately 75 m.

Internal wave energy flux is estimated as $\mathbf{F} = \langle \boldsymbol{u}' p' \rangle$, where $\boldsymbol{u}'$ is the internal wave velocity perturbation (u', w'), p' is the internal wave pressure perturbation, and the brackets denote a time average (Kang & Fringer, 2012). The full expression for $\mathbf{F}$ includes additional terms for advection and diffusion, and in a

field setting on the California coast, Kang and Fringer (2012) found that these terms contribute less than 1% to the total energy flux budget. In this present study, where we have no barotropic currents in the model, these additional terms are expected to be very small and are neglected.

3. Results

3.1. Origins of the Internal Waves Observed at Dongsha Atoll

The amplitude and timing of internal waves in coastal waters are often difficult to predict given that internal waves may originate from multiple generation sites and conditions (currents and water density stratification) through which they propagate (Nash et al., 2012). However, the origins and properties of the large-amplitude ISWs in the northern South China Sea are relatively well constrained by past observations and modeling (Alford et al., 2015; Alford et al., 2010; Buijsman et al., 2010; Hsu & Liu, 2000; Klymak et al., 2006; Ramp et al., 2010; Simmons et al., 2011; Zhang et al., 2011; Zhao & Alford, 2006; Zhao et al., 2014), and the timing of their arrival on the narrow Dongsha shelf can be traced back to tidal currents in the Luzon Strait generation region (Figure 1d and 1e). The arrival of the largest internal waves incident on the Dongsha shelf, as indicated by sudden, large drops (4–10 °C in <1 min) in water temperature, generally occurs within 1 h of the predicted arrival time of Luzon-generated waves (based on a predicted 50-h lag from maxima in Luzon tidal currents and propagation speeds of 2–3 m s^{-1} over ~500-km distance) (Alford et al., 2010; Ramp et al., 2010). Internal wave-driven cooling on the shallow slope is larger in the two days following spring tides (4 June and again on 16–17 June in our observations, Figure 1e) than following neap tides (9–10 June in Figure 1e), although there are exceptions. There is no one-to-one correspondence between maxima/minima in Luzon tidal currents (forcing) and arrival of internal waves on Dongsha, and this could be due to several factors: weaker tidal currents during neap tides within Luzon Strait may not generate ISWs (Ramp et al., 2010) (e.g., Figure 1e shows small temperature drops between 2–5 and 12–14 of June that are associated with weaker flood beats in Figure 1d), the largest ISWs may break down into a train of smaller-amplitude and higher-frequency internal waves (Duda et al., 2004; Fu et al., 2012; Orr & Mignerey, 2003), or the internal waves may interact with the Kuroshio current or mesoscale eddies along the propagation path (Li et al., 2016). There may also be some local generation of internal waves with the local internal tide interaction with the slope, but the strong correspondence seen in our data with the Luzon-originated waves suggests that this contribution is likely small.

In addition to ISW arrivals, nearly continuous, smaller-amplitude temperature fluctuations (1–4 °C) are associated with higher-frequency internal waves that may be generated locally or at a different remote location, and their arrival times are thus not correlated with tidal currents in the Luzon Strait. The ISWs in Figure 1e are superimposed on a tidal timescale fluctuation in water temperature imposed by the local internal tide. A cooling trend in fore reef waters during 13–17 June 2014 is related to the strong winds of tropical cyclone Hagibis (Figure 1e).

3.2. Spatially Continuous Measurements of Internal Waves

Internal waves perturb the temperature and density structure of coastal waters, but the nature of the perturbation depends upon the form and amplitude of the waves. Here, we combine spatially continuous measurements of near-bed temperature from the DTS with observations of currents and vertical structure of the water column by a suite of instruments deployed at Mooring E1 (Figure 2) to examine the form of the internal waves on Dongsha Atoll, their propagation path, phase speed, onshore extent, and retreat back down the slope.

The DTS data provide a unique, quasi-3D view of continuous near-bed temperature measurements across 700 m of the Dongsha inner shelf (Figure 2). Sharp, cold temperature fronts (blue and green streaks in Figure 2a) are internal wave fronts propagating upslope (from bottom to top in the figure) over time. A total of 543 internal waves were detected over 11 days (2–12 June), averaging two waves per hour (but waves were not evenly spaced in time).

3.2.1. Upslope Evolution

From previous observations in the Dongsha Plateau shelf region, we know that as the large ISWs advance on the continental slope, they can develop into a train of waves, some with trapped cores (i.e., a recirculating mass of fluid transported with the wave) (Lien et al., 2012; Orr & Mignerey, 2003). Over the steep topography
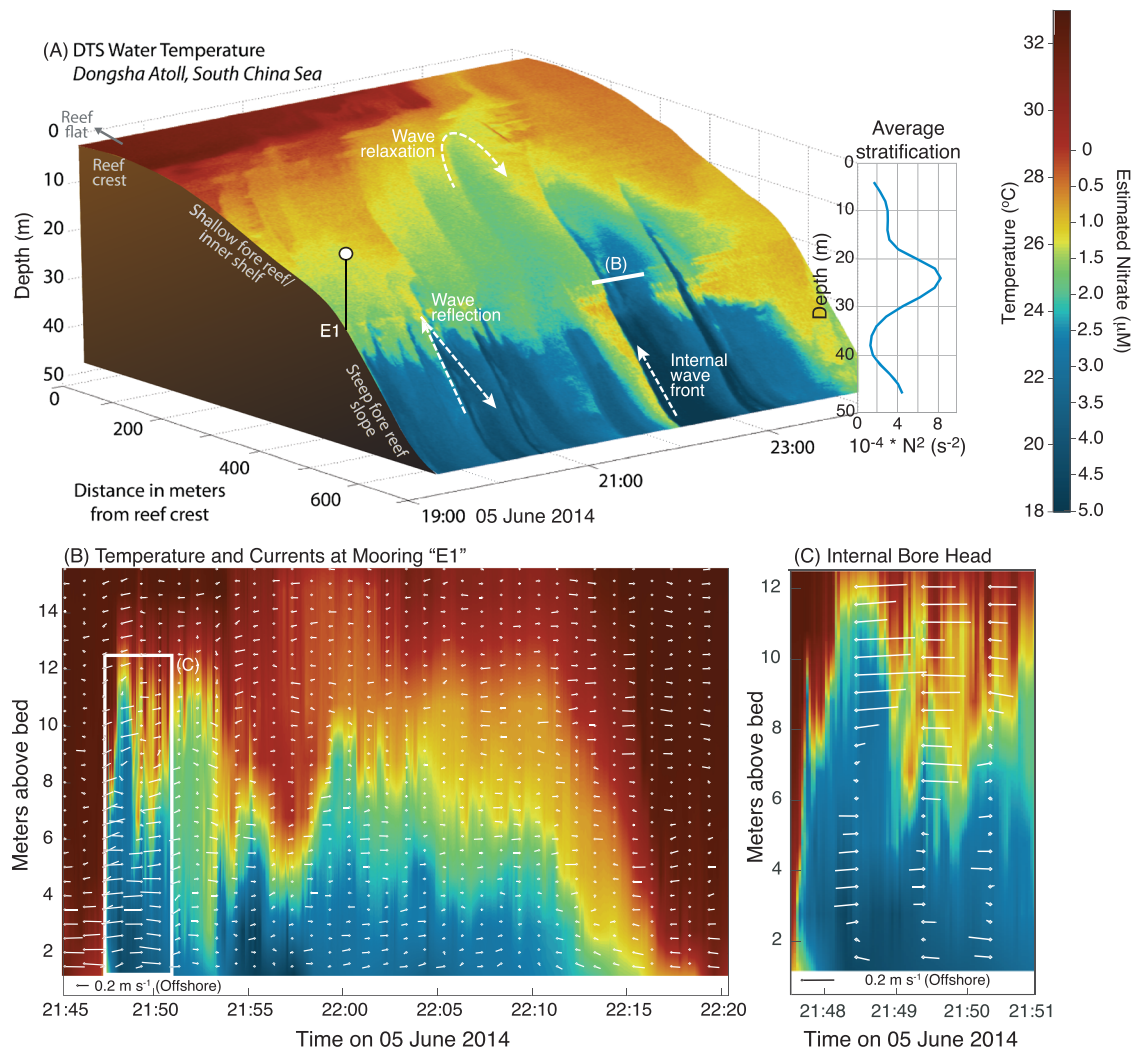
Figure 2. Nonlinear internal waves on the inner shelf. (a) Example of DTS data for 6 h on 5 June 2014 (representing ~200,000 independent temperature measurements). Quasi-3D plot shows near-bed temperatures from DTS and estimated nitrate concentration from the reef crest (~2-m depth) to the offshore terminus of the cable (~50-m depth). Examples of the DTS signature of an internal wave (of elevation) front, wave reflection, and wave relaxation are indicated with white dashed lines. Time-averaged stratification (N^2) for the study period is shown to the right of the DTS data (blue line). The location of Mooring E1 on the slope and the duration and location of the time series shown in panel (b) are also indicated. (b) Vertical array of water temperature (same color scale as in panel a) and the vertical and across-shore components of velocity in a stationary reference frame (aspect ratio of velocity quivers is 1:1) at Mooring E1 for 35 min corresponding to the solid white line in panel (a). (c) Enlarged view of the head of the solibore (white boxed region of panel b). Quivers represent velocities in a reference frame moving with the apparent phase speed of the bore (0.18 m s^{-1}), showing circulation within the core of the solibore head.

east of Dongsha Atoll, they transform rapidly from solitary waves of depression in water depths >400 m to waves of elevation with amplitudes roughly 100–150 m in water depths <200 m (Fu et al., 2012). Satellite images (hyperspectral images as in Figure 1b and synthetic aperture radar images such as in Figure 6 of Guo and Chen, 2014) show evidence of significant refraction and reflection of internal waves around Dongsha Atoll.

Upon reaching water depths <50 m, the internal waves are in the form of highly nonlinear solibores and boluses and are associated with an upslope-propagating cold temperature front in the DTS data (white arrow indicating "internal wave front" in Figure 2a) and the onshore flux of dense, cold water in the bottom ~10 m of the water column, as seen in a representative solibore event passing E1 at 21:48 (Figure 2b). The apparent phase speed (c_p, estimated from the DTS wave characteristic and explained in detail in section 3.2.5) of this bore is relatively constant on the steep slope below 25 m (0.43 m s^{-1}), but slows quickly as it moves up the
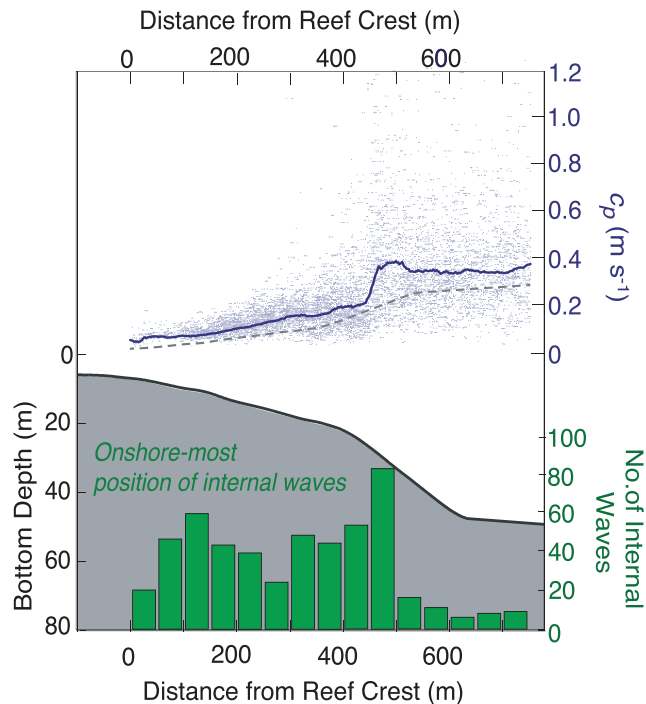
Figure 3. Smoothed across-shore bathymetry of the Dongsha east fore reef with instantaneous estimates of apparent internal wave phase speed (blue dots) and averaged phase speed over all internal waves (blue line). For reference, a long, linear, first-mode internal wave speed is shown (dashed gray line). Green bars indicate the location of the onshore-most extent of internal waves as detected in DTS data.

slope past E1 (0.18 m s^{-1}), eventually losing its onshore momentum around 200 m offshore of the reef crest. Apparent phase speed and the onshore-most position for all events detected with the DTS between 2–12 June 2014 are shown in Figure 3. Many of the events detected in the DTS data exhibited a cold (blue) track of discrete cross-shore spatial extent (~20–40 m in apparent length), which suggests the existence of a trapped core of cold water (e.g., Figure 5a).

The detailed velocity and temperature structure of the representative solibore event at E1 over a 30-min period shown in Figure 2b exhibits features characteristic of both a nonlinear ISW of elevation with a trapped core and of an internal bore with a tail of dense fluid. A sharp front of cold water (8 °C drop in 15 s) at 21:48 marks the head of the solibore, with onshore velocities of 0.3 m s^{-1} within the cold core and strongly sheared velocities near the top of the solibore head (offshore directed). The strong onshore velocity in the head of the solibore (0.3 m s^{-1}) significantly exceeds the front propagation speed at Mooring E1 (0.18 m s^{-1}, estimated from the DTS), suggesting the existence of a trapped core.

In an enlarged view of the head (Figure 2c), there is evidence of large density overturns (~ 4 m high) in the strongly sheared region near the top of the solibore head (6–10 m above the bed). Further evidence for a trapped core can be seen in the recirculating pattern of currents within the cold head of the solibore at 21:48 in Figure 2c., which shows velocities in a reference frame moving with the apparent phase speed of the bore front as it passes E1 (Helfrich & White, 2010). Very near the bed (<2 m above the bed, in Figure 2c), there is evidence of a small region of reverse circulation (offshore flow) within the head of the solibore similar to that seen in simulations of bolus propagation on a shelf (Venayagamoorthy & Fringer, 2007), which may allow dense water to leak out of the back of the trapped core.

A region of relatively well-mixed temperature fluid follows the head (the green patch between 4 and 10 m above the bed, to the right of the white box in Figure 2b), partially separating the head from the tail of the solibore. This region of elevated mixing could be created by an adverse pressure gradient or large-scale vortices (not resolved by our velocity measurements) shedding off of the strongly sheared region in the solibore head as seen in numerical simulations of shoaling ISWs of elevation (Diamessis & Redekopp, 2006; Stastna & Lamb, 2008) and could be contributing to the formation of the trapped core in the head region. The cold-water tail of the solibore continues to propagate onshore past Mooring E1 from 21:53–22:09, where it loses onshore momentum and the dense water relaxes back offshore.

3.2.2. Internal Wave Reflection

Evidence of internal wave reflection off of the Dongsha shelf has been documented in satellite images and predicted in numerical simulations of the shelf slope region (Bai et al., 2017; Guo & Chen, 2014). Bai et al. (2017) estimated that as much as 20% of incident internal wave energy may be reflected back offshore. Many of the internal waves tracked with the DTS were reflected off the steepest section of the slope (the bottom slope just offshore of E1 is 0.15): distinctive "V"-shaped formations in the temperature data indicate a rapid change in direction for the internal wave (see example in Figure 2a) and are consistent with previous observations of internal waves reflecting on a natural slope (Bourgault et al., 2011). Both the onshore and offshore "legs" of the V-shaped temperature pattern are sharp temperature gradients, giving some indication that a coherent wave form is maintained throughout the reflection process (Bourgault et al., 2011). However, the apparent phase speed of the reflected waves is, on average, 60% slower than the incident waves, suggesting a loss in energy during reflection. The reflection of internal waves of elevation off of sloping bathymetry has been documented in laboratory studies and is consistent with the near-bed temperature pattern observed here (Chen et al., 2007).

3.2.3. Internal Wave Relaxation

Internal waves that are transmitted onshore of the steepest slope (onshore of E1) eventually lose their onshore momentum, and the dense water transported upslope by solibores and boluses gradually accelerates back offshore in a relaxation phase. This relaxation phase is visible as "U"-shaped patterns in the DTS temperature contours (see example in Figure 2a), with progressively less distinct temperature gradients due to turbulent mixing, which continues throughout the shoaling process (Davis & Monismith, 2011; Walter et al., 2012).

3.2.4. Internal rundown

As internal waves shoal at Dongsha, a strong offshore-directed jet is consistently observed near the bed, with a coincident onshore flow of warmer water in the upper part of the water column (Figures 2a and 2b). In many cases, these downslope jets have a strong effect on the water column structure over the slope. For example, just prior to the cold front of the reference wave (indicated by the white arrow labeled "Internal wave front" in Figure 2a and in Figure 2b at 21:47), a strong downslope jet pulls water of near-surface temperature (27 °C) down to 40-m depth on the steep fore reef slope. Strong downslope flow preceding a shoaling ISW, "internal rundown" (a term adopted from surface wave nomenclature), has been seen in laboratory experiments (Michallet & Ivey, 1999; Nakayama & Imberger, 2010; Umeyama & Shintani, 2006) and numerical models (Aghsaee et al., 2010; Arthur & Fringer, 2014) as well as in the field (Bourgault et al., 2005; Fu et al., 2012; Scotti & Pineda, 2004). This downslope flow occurs as the leading depression phase of the ISW interacts with the bathymetry and near-bottom water is pulled down the slope prior to the arrival of the wave of elevation that has formed from the steepened rear face of the ISW. The dynamic internal wave field of the Dongsha slope makes it challenging to isolate internal rundown from the relaxation phase of the previous wave. However, the intensity of the observed downslope jets (in some cases up to 0.45 m s^{-1} within a meter of the bed at Mooring E1) suggests that the gravitational flow of dense fluid down the slope from the previous wave may not be the only driving force for the observed near-bed current. For example, observed stratification and near-bed jet dimensions related to the reference wave in Figure 2 were used to estimate the speed of a gravity current on a sloping bed (β~3–5° for the slope shoreward of mooring E1) as $U_{grav} = \sqrt{\frac{g' h \sin \beta}{C_d}}$, where $g' = g\rho/\rho$ is reduced gravitational acceleration calculated by a representative density (ρ) difference between fluids, h is the depth of the gravity current, and C_d is the coefficient of drag estimated from nearby measurements of flow over the reef flat (Reid et al., 2019). Estimates of U_{grav} are 0.18–0.22 m s^{-1}, which is consistent with the offshore-directed, near-bed velocities observed at the end of the bore (0.16–0.18 m s^{-1} at 22:15–22:20 in Figure 2b), but significantly slower than the downslope jet that precedes the arrival of the solibore head (0.35 m s^{-1} at 21:45–21:46 in Figure 2b). This suggests that the strong, bottom-intensified offshore jet preceding the wave is driven, at least in part, by internal rundown. We examine this mechanism further using idealized numerical simulations in section 4.1.

3.2.5. Variable Propagation Speed of Nonlinear Internal Waves Across the Shelf

The phase speeds of the internal waves were estimated from the wave characteristic lines as $c_{ph} = dx/dt$, where dx is the change in cross-shore distance and dt is the change in time. This method assumes that the dense fluid within the core is traveling up the slope at the same speed as the wave front (even though velocities within a trapped core may exceed the wave speed). This assumption is tested below in numerical simulations of a "virtual DTS" (section 4.1). Based on digitization and analysis of the DTS data, we estimate the phase speed of observed internal waves—both incoming and reflected—as well as the onshore terminal position of each wave (Figure 3). Below 25-m depth on the steep slope, the onshore component of the speed of observed internal waves is approximately constant at 0.36 m s^{-1} (Figure 3), 20% faster than a linear, first-mode internal wave speed (gray dashed line in Figure 3; see section 2.3 for further details on calculation). As the bores and boluses run up past the topographic slope change at 25-m depth (near E1), they slow in speed (see also Figure 2a). Along this gentler portion of the bed slope, the temperature gradient becomes less sharp as the cold fluid within the bolus mixes with the ambient temperature water. Eventually, the boluses lose their onshore momentum, leading to the relaxation of cold water back down the slope.

4. Discussion

4.1. Comparisons With Numerical Modeling

A 2D semi-idealized numerical model using realistic bathymetry and stratification is used to complement the DTS observations and to explore how the internal wave structure and dynamics over the entire water
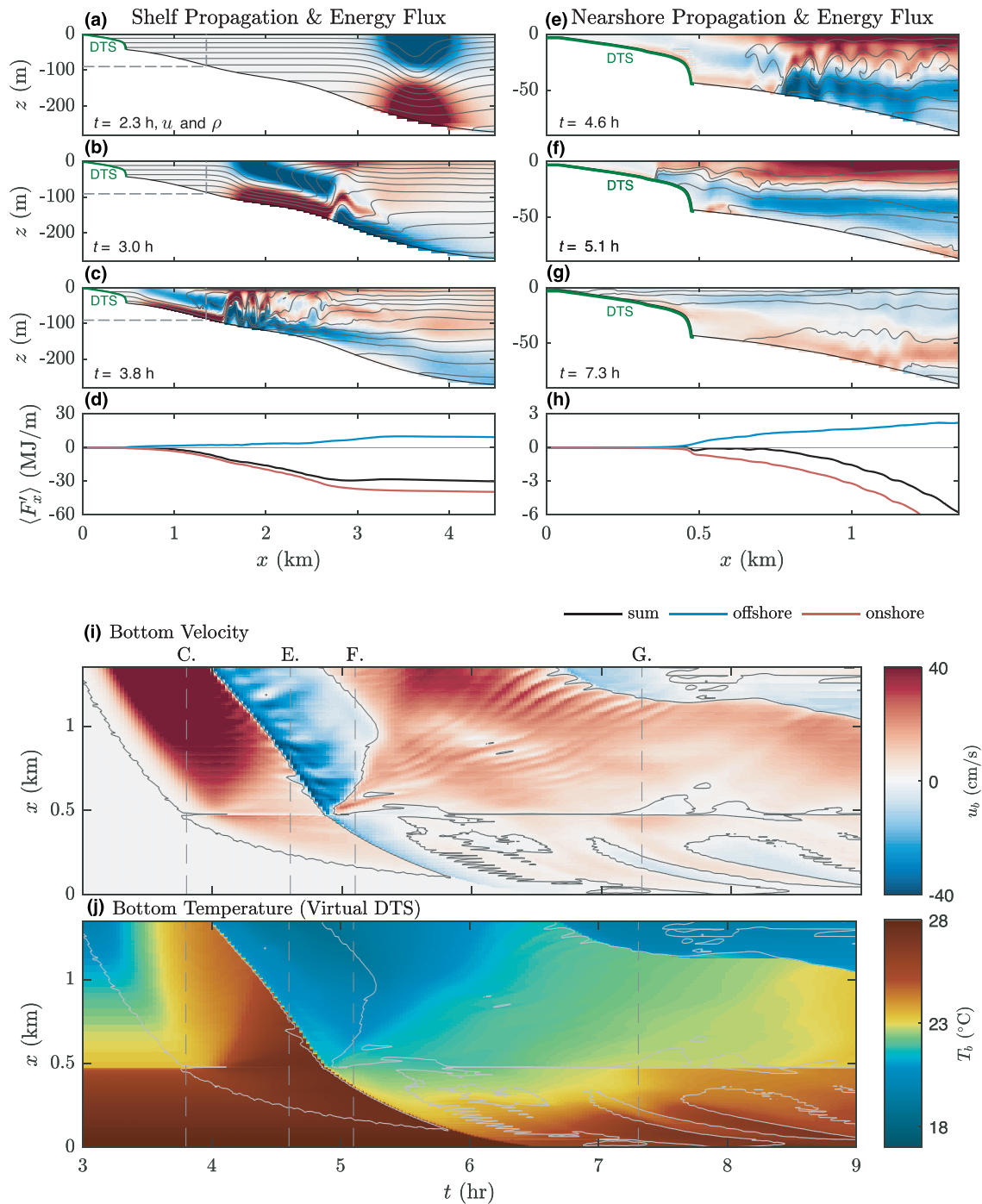
Figure 4. Numerical simulation of internal wave on Dongsha atoll. (a, b, c, e, f, g) Snapshots of cross-shore density structure and across-shore component of velocity (positive u is offshore-directed flow) from a SUNTANS simulation. Green line on slope corresponds to the location of the field deployment of the DTS instrument. (d, h) Onshore-directed (red), offshore-directed (blue), and total (black) internal wave energy flux integrated vertically and over the period of the internal wave. (i) Near-bottom, across-shore velocity, u_b, and (j) near-bed water temperature ("virtual DTS") plotted over the slope and period of internal wave shoaling. Vertical dashed lines in (i and j) correspond to snapshots of time in panels (a, b, c, e, f, g). Contour lines in (i and j) are for $u_b = 0$.

column might lead to the observed patterns in the DTS temperature data (Figure 4). In the numerical run, a solitary wave of depression propagates onshore (Figure 4a) where it begins to interact with the slope. This interaction causes a strong downslope flow near the bed ("internal rundown") and steepening of the rear face of the wave (Figure 4b). A solitary wave of elevation then forms on the steepening rear face of the
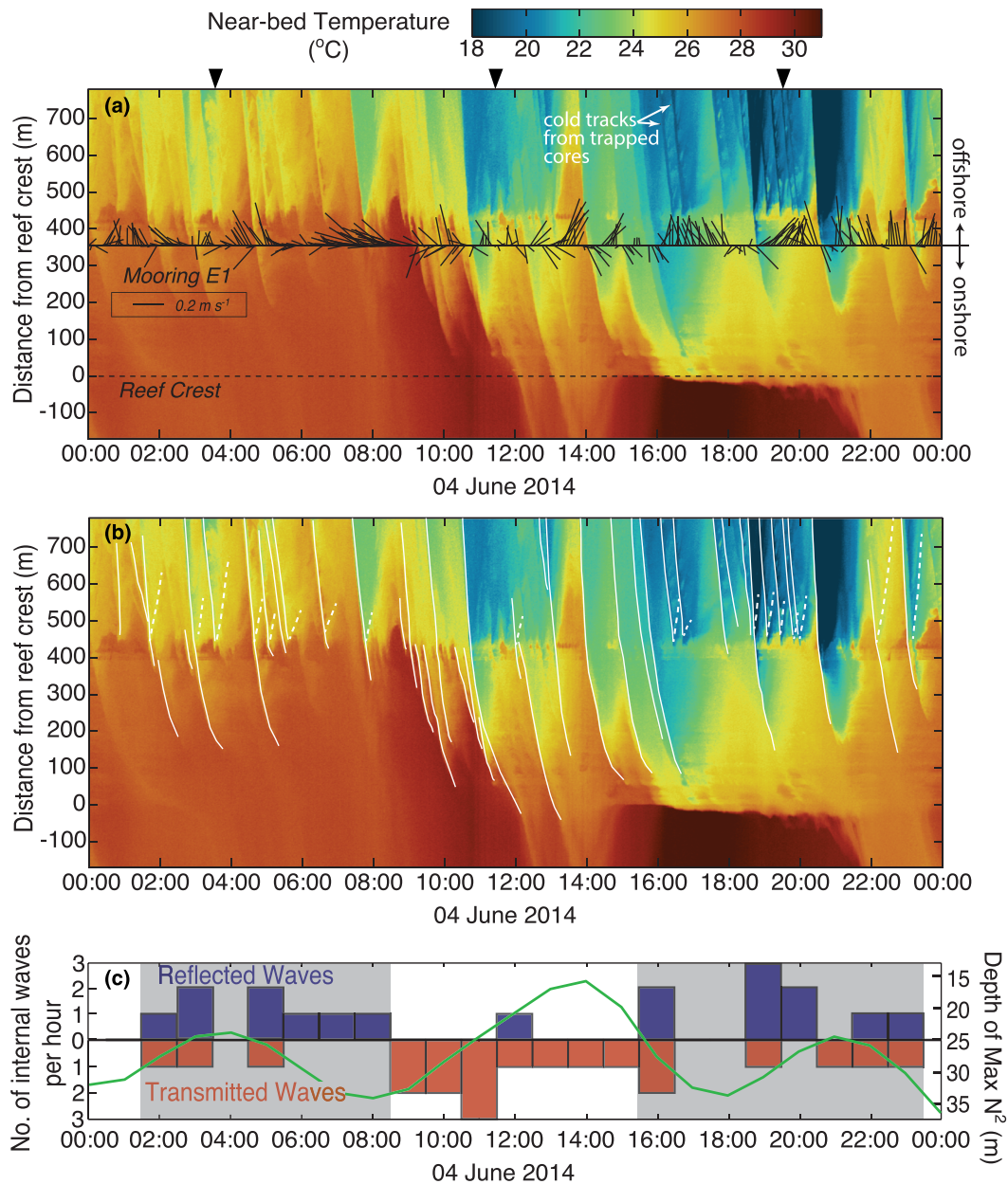
Figure 5. (a) Near-bed temperature from DTS measurements for 24 h on 4 June 2014. Dotted line indicates location of reef crest (~2-m depth) and quivers show velocity 1 m above the bed (black) at Mooring E1. Note: Color bar in Figure 5 is different from Figure 4. Black triangles at top indicated the predicted arrival time of waves generated in Luzon Strait. Incoming waves are the yellow, blue, and green streaks extending downward and to the right, whereas downslope flow events (relaxation or internal rundown) are marked by yellow and orange streaks projecting upward and to the right. (b) Same as in (a), but with wave characteristics highlighted. Solid white lines and dashed white lines indicate incident and reflected internal wave-induced temperature fronts, respectively. (c) Number of internal waves reflected offshore of steep slope (blue bars) and transmitted onshore of Mooring E1 (red bars) for each hour of 4 June 2014. 1-h low-pass filtered depth of the maximum buoyancy frequency (green line).

initial wave of depression (Figure 4c) and propagates onshore as a dense bore with large instabilities forming behind the head of the bore (Figures 4c and 4e). Additionally, some of the internal wave energy is partially reflected off of the steep reef slope (near 0.4 km from the reef crest), causing a reversal in the flow direction near the bed (Figure 4f).

The numerical simulation was used to create a "virtual DTS": a plot of density in the bottom-most grid cell as a function of cross-shore distance (*x*) and time (*t*) (Figure 4j). The key features and behaviors of waves

observed in the field are also evident in the model-derived virtual DTS. For example, the virtual DTS shows warm water drawn offshore and downslope ahead of the incident internal wave (internal rundown; $t = 3.5$– 4 h or "C" in Figures 4i and 4j), followed by the same form of wave observed at E1 in Figure 2: an onshore-directed front of dense water, marking the head of an internal bore, surges upslope ($t = 4.25$– 6.5 h, or "E" and "F" in Figures 4i and 4j). A V-shaped reflection off of the steep section of the slope (just before $t = 5$ h in Figures 4i and 4j) matches the DTS signature and location of the internal wave reflections seen in observations (Figure 2a, see also Figures 5a and 5b). Gradual rewarming of the slope is also seen in the model, with a prolonged period of offshore flow and the "U"-shaped relaxation of dense water back down the slope in the model ($t = 5$–7 in Figure 4j).

Because the model shows a single shoaling internal wave on an initially quiescent slope, the results also help to isolate the internal rundown (before) and relaxation (after) phases of shoaling waves that are difficult to separate in our field observations. The model results thus support our hypothesis that internal rundown is contributing to the downslope current just before the arrival of a large-amplitude internal wave.

We can also directly compare the phase speed of the shoaling waves in the model with the slope of the onshore-propagating dense front seen in the virtual DTS. The average phase speed of the modeled internal bore from $0.5 < x < 1.3$ km is $c_p = 0.3$ m s^{-1}, which agrees well with the virtual DTS estimate (slope of the density front in distance-time space) as well as the observed DTS apparent phase speed averaged over all internal wave paths offshore of the slope break (Figure 3).

Internal wave energy flux is integrated in time (over the entire period of the wave shoaling and reflection, from $t = 0$ to $t = 9$ h) and over the depth of the water column, as $F'_x = \iint (u'p') \, dz \, dt$ (Figures 4d and 4h). Because the simulation contains one wave event, we approximate negative wave energy flux when $\int (u' p') \, dz < 0$ (primarily beginning of the simulation) and positive energy flux as times where $\int (u' p') \, dz > 0$ (primarily end of the simulation). Results from this simple 2D numerical experiment suggest that approximately 70% of the incident internal wave energy is dissipated after the wave breaks into a wave of elevation and, eventually, an internal bore ($0.5 < x < 3$ km). The reflection coefficient, R, defined as the ratio of the reflected to incident wave energy, was estimated for the modeled internal wave at a point far offshore of the reflection ($x = 6$ km) as 0.21, a value consistent with the estimate of energy reflected from Dongsha Atoll by Bai et al. (2017).

Compared with the energetic wave environment offshore, very little internal wave energy makes it to the shallow reef since much of it is dissipated along the slope in depths >100 m (Figure 4d) and much of the remaining energy is reflected at $x = 0.5$ km (Figure 4h). Nevertheless, the overall effect of the wave is to deflect the isopycnals upward in the shallows and draw the cooler water up to the reef. And, while a significant fraction of the incident internal wave energy is reflected off of the steep slope at $x = 0.5$ km, some energy is transmitted shoreward, as evidenced by the cold bore that propagates eventually all the way to the reef crest ($x = 0$) in the simulation (as well as in observations, e.g., Figure 5a).

The bands in the plot of bottom across-shore velocity (Figure 4i) around $5 < t < 8$ h represent offshore-directed internal waves, which are a result of the unsteadiness created by the internal bore colliding with the steep section of the slope at $x = 0.5$ km. The propagating bore creates many deflections to the density in its wake, and these forms propagate away as a series of nonlinear waves (Figures 4e and 4i).

4.2. Fate of Internal Waves on the Inner Shelf

Ultimately, the influence of internal waves in nearshore environments is determined by the fraction of wave energy that is transmitted onto the shelf, where it can transport deep water masses shoreward or drive mixing inshore of the shelf break, versus reflected off the slope, where the energy is dissipated in deeper waters. The limitations of this observational data set for evaluating the fate of internal wave energy on the Dongsha shelf are twofold: first, the one-dimensional aspect of the FO cable deployment does not allow for detection of the alongshore component of the wave speed (see section 2.2 for detailed discussion) or other alongshore variability in dynamics; second, Mooring E1 lacks measurements of velocity and water column structure in the top third of the water column, preventing a reasonable estimate of the nonlinear terms of the internal wave energy flux (Nash et al., 2005; Scotti et al., 2006). Nevertheless, the spatially continuous perspective of the DTS data, paired with the vertical array at E1 allows us to track the cross-shelf path of internal

waves on Dongsha—which at this location on the shelf are largely bottom-intensified waves of elevation or internal solibores—and examine the dynamic conditions controlling their fate.

Of the total internal waves (543) detected by the DTS over the 11-day deployment, a subset of 233 internal waves was tracked to determine how their fate (i.e., transmitted onshore of E1 or reflected offshore of E1) was related to background conditions (stratification and currents on the shelf). This subset of tracked waves contained waves that occurred during the 9-day period of overlap in DTS and Mooring E1 measurements and waves that could be detected in the DTS within 100 m of Mooring E1. In addition to the 233 internal waves we categorized, 40 waves detected onshore of Mooring E1 did not have a temperature signature offshore of the shelf break, perhaps because their amplitudes were too small to detect in deeper water with the cable located on the bed or because they were generated during the breaking of another wave on the steep slope.

In some cases, an incident internal wave is partially reflected offshore and partially transmitted past the slope break—a partitioning of internal wave energy that is expected from theory. Examples of this can be seen in Figure 5b at times 01:00–05:00, where an incident wave corresponds to a thermal front propagating both offshore (dashed white line) and onshore (solid white line) of the steep slope. In the case of partial reflections, the wave was counted as both reflected and transmitted. Strictly speaking, it is likely that none of the incident internal waves are perfectly transmitted or reflected from the shelf as they are already highly nonlinear events and are dissipating energy as they shoal shoreward. Here, however, we will assume that the path described by the strongest thermal fronts is the primary direction of internal wave propagation and energy flux.

As an example of the patterns of wave reflectance and transmittance, we first focus on 4 June 2014 (Figure 5). A total of 42 internal waves were observed during this 24-h period. Strong near-bed flows (black quivers at E1 in Figure 5a) are associated with the onshore propagation (onshore flows) and relaxation or rundown phases (offshore flows) of the internal waves. Figure 5b shows the wave characteristic lines estimated from DTS measurements (see details in section 3.2.5), and Figure 5c shows the corresponding counts of waves reflected (blue bars) and transmitted (red bars) past the slope break at 25-m depth (i.e., mooring E1) for each hour of the time series. Between 02:00–08:00 GMT and again between 16:00–23:00 GMT (gray shaded regions in Figure 5c), 17 reflected waves were detected and only 9 were transmitted onshore, while in the intervening period between 09:00–15:00, only 1 reflected wave was detected and 11 transmitted, in some cases bringing cool water all the way past the reef crest at $x = 0$ (Figures 5a and 5b). This time series highlights how dramatically the fate of internal wave energy incident on the steep fore reef can change at time scales shorter than a day. In total over the 11-day deployment, 76% of the internal waves analyzed had a clean transmission past the slope break at 25-m depth with no detectable reflection; 18% reflected back offshore on the steep slope with no detectable thermal front onshore of the slope break; and 6% had a partial reflection with a detectable thermal front heading both onshore and offshore of the slope break.

The breaking-type and reflectance properties of ISWs and their run-up structure on the shallow shelf are dependent upon the characteristic length scales of the incoming wave and topographic slope. These length scales have typically been classified using a dimensionless ratio of the bathymetric slope, s, to the wave steepness, quantified in the internal Iribarren number as $\xi = s/\sqrt{a/\lambda}$, where a is wave amplitude and λ is the wavelength (Aghsaee et al., 2010; Boegman et al., 2005a; Iribarren & Nogales, 1949; Shroyer et al., 2009). Dongsha has a relatively steep bathymetric slope (0.03–0.15), but the incident internal waves can also be quite steep (Fu et al., 2012) ($a/\lambda \sim 0.3$–0.7), resulting in a wide range of ξ (0.1–0.9) for incoming waves.

In our observations, the strength of water column stratification (i.e., vertically averaged N^2) was not significantly different in magnitude for periods with reflected versus transmitted waves, but the vertical position of the pycnocline (region of maximum N^2) was deeper during periods with reflected internal waves compared with times without (Figure 5b), suggesting that the vertical position of the pycnocline relative to the depth of the slope break and the steep section of the slope below it may govern the transmission or reflection of incident internal waves (Hall et al., 2013). This idea is supported by laboratory and numerical experiments on interfacial waves in a two-layer fluid, which find that the degree of "blocking" (B) of a topographic obstruction is an important factor controlling the scattering of energy into transmitted and reflected waves (Diebels et al., 1994; Vlasenko & Hutter, 2001; Vlasenko & Hutter, 2002; Wessels & Hutter, 1996). When $B < 1$, the top of the obstruction is completely within the lower layer (below the undisturbed density interface), while $B > 1$
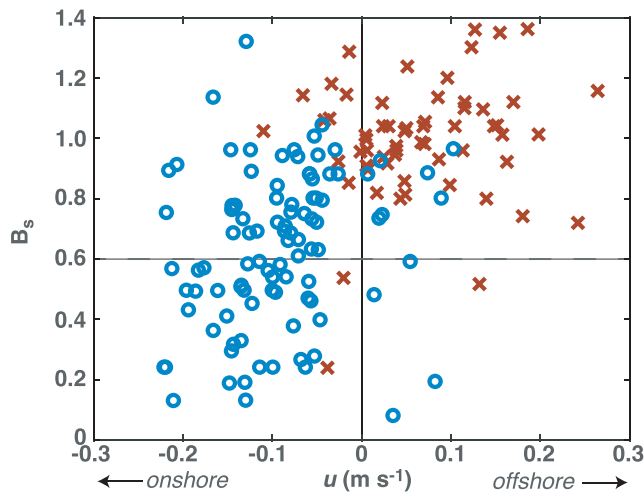
Figure 6. Blocking parameter, B_s, versus near-bed cross-shore currents vertically averaged from 1–4 m and for 5 min before wave arrival at slope break. Each point represents a transmitted (**O**) or reflected (**X**) internal wave. The horizontal dashed line represents $B_s = 0.6$, the limit found in laboratory experiments, below which an incident wave is essentially transmitted past an obstruction without much reflection.

means that the obstruction reaches into the upper layer. We can define the blocking parameter using surface-referenced depths, as $B_s = H_1/d$, where d is the depth of the top of the obstruction (in this case, d is the depth of the slope break at 25 m) and H_1 is the upper layer depth (defined here to be the depth of maximum N^2). Both laboratory and numerical studies (referenced above) found that for $B < 0.6$, an incident wave is essentially transmitted past the obstruction without much scattering of energy, while for $B > 0.8$, a partial refection of the wave becomes apparent, and total reflection is possible for B greater than 1.

In the highly dynamic internal wave field incident on Dongsha Atoll, the vertical position of the pycnocline changes significantly over the timescale of hours (Figure 5b) either due to the phase of the local internal tide or due to higher-frequency modifications of the local stratification from a preceding internal wave. On 4 June 2014, the periods of time with many observed reflections (e.g., 02:00–08:00 and also 16:00–23:00) were associated with a pycnocline positioned deeper than the top of the slope break (~25 m) or a blocking parameter $B_s > 1$, while in the 7-h period with only one observed reflection, the pycnocline was shallower, as high as 16 m. This pattern is consistent with the full 9-day analysis period where reflected waves are associated, generally, with a larger blocking parameter (average for all 70 reflected waves analyzed $B_s = 0.99$) than internal waves transmitted to the inner shelf (average $B_s = 0.63$ for 133 internal waves traced from offshore to onshore of E1) (Figure 6). Some internal waves transmitted to the inner shelf were also associated with a high blocking parameter ($B_s > 0.6$). However, these waves, on average, had 34% higher phase speeds than the incident waves that were eventually reflected and thus were likely higher-amplitude ISWs capable of overcoming the slope break obstacle despite the localized depression of the pycnocline.

The presence of a background current can also change the amplitude, speed, and breaking point of shoaling internal waves, and this influence is most pronounced when the maximum shear layer is aligned with the center of the pycnocline (Stastna & Lamb, 2002). The offshore-directed jets common to the Dongsha fore reef slope likely create strong shear conditions at the slope break region, which is also located at the same depth as the maximum stratification (~25 m) during the June 2014 experiment and is thus likely to modify the characteristics of internal waves approaching the shelf. It may be that strong offshore and downward-directed (due to the slope angle) currents act to depress the thermocline at the slope break, encouraging the interaction of the following waves with the steepest section of the slope. For example, reflected waves detected in the DTS data were primarily associated with near-bed, offshore-directed currents on the shelf just prior to their arrival at the steepest part of the shelf (Figure 6). On 4 June 2014, we can see examples of this in the DTS and current meter data for internal wave events at approximately 16:30 and 19:00 (Figure 5b). The leading internal wave in these packets is transmitted to the inner shelf (past E1), and the relaxation of this dense water back offshore creates a near-bed jet of water (black quivers pointed upwards). Internal waves arriving at the steep shelf break during the strong offshore flow are reflected back offshore until a larger-amplitude wave capable of overcoming the local slope break conditions arrives on the slope.

We conclude that the transformation and path of internal waves incident on the Dongsha slope are dependent upon the highly dynamic stratification and near-bed currents at the slope break. Our observations suggest that the stratification and current conditions on the shelf are strongly influenced by previous shoaling internal waves, highlighting the importance of wave-wave interactions for inner shelf internal wave dynamics.

4.3. Consequences for Coastal Ecosystems

The spatially continuous perspective of temperature afforded by the DTS instrument reveals that internal waves, often thought of as deep-ocean phenomena, are not uncommon in shallow coastal waters, transporting heat (or cold) and nutrients to coastal benthic communities and creating small-scale physical variability in the benthic environment (Leichter et al., 2003; Stokes et al., 2011).

At Dongsha Atoll, the internal wave delivery of nutrients nourishes a shallow reef community (Wang et al., 2007), likely contributing to what has been recently reported as the fastest calcification rate found to date on any reef system (DeCarlo et al., 2017). Nitrate concentrations estimated from temperature (Figure 2a, see section 2.4 for details) illustrate how nutrient-rich water is periodically pushed up onto the shallow fore reef slope by internal waves. For example, in the trapped core of the example internal solibore (Figure 2b), nitrate concentrations reach up to 3 μM, greatly elevated above levels typical of the oligotrophic northern South China Sea.

Future work can build on the methods we have introduced to quantify the spatial distribution of energy, heat, and nutrients across the shelf, investigate wave-wave interactions, and assess seasonal or interannual variability of internal wave influence in nearshore regions of the South China Sea and elsewhere. Given the impending changes in climate (including changes in ocean stratification, sea surface temperatures, oxygen, and pH), the presence, magnitude, and periodicity of internal waves may ultimately be a critical factor in the health and persistence of coastal ecosystems such as the coral reef at Dongsha (DeCarlo et al., 2015; Schmidt et al., 2016; Tkachenko & Soong, 2017; Wall et al., 2015).

References

Aghsaee, P., Boegman, L., & Lamb, K. G. (2010). Breaking of shoaling internal solitary waves. *Journal of Fluid Mechanics*, *659*, 289–317.

Alford, M., Peacock, T., MacKinnon, J. A., Nash, J. D., Buijsman, M. C., Centuroni, L. R., & Fu, K. H. (2015). The formation and fate of internal waves in the South China Sea. *Nature*, *521*(7550), 65–69. https://doi.org/10.1038/nature14399

Alford, M. H., Lien, R.-C., Simmons, H., Klymak, J. M., Ramp, S., Yang, Y.-J., et al. (2010). Speed and evolution of nonlinear internal waves transiting the South China Sea. *Journal of Physical Oceanography*, *40*(6), 1338–1355.

Arthur, R., & Fringer, O. (2014). The dynamics of breaking internal solitary waves on slopes. *Journal of Fluid Mechanics*, *761*, 360–398.

Arthur, R. S., Koseff, J. R., & Fringer, O. B. (2017). Local versus volume-integrated turbulence and mixing in breaking internal waves on slopes. *Journal of Fluid Mechanics*, *815*, 169–198.

Bai, X., Li, X., Lamb, K. G., & Hu, J. (2017). Internal solitary wave reflection near Dongsha Atoll, the South China Sea. *Journal of Geophysical Research: Oceans*, *122*, 7978–7991. https://doi.org/10.1002/2017JC012880

Boegman, L., Ivey, G. N., & Imberger, J. (2005a). The degeneration of internal waves in lakes with sloping topography. *Limnology and Oceanography*, *50*(5), 1620–1637.

Boegman, L., Ivey, G. N., & Imberger, J. (2005b). The energetics of large-scale internal wave degeneration in lakes. *Journal of Fluid Mechanics*, *531*, 159–180.

Bourgault, D., Blokhina, M., Mirshak, R., & Kelley, D. (2007). Evolution of a shoaling internal solitary wavetrain. *Geophysical Research Letters*, *34*, L03601. https://doi.org/10.1029/2006GL028462

Bourgault, D., Janes, D. C., & Galbraith, P. S. (2011). Observations of a large-amplitude internal wave train and its reflection from a steep slope. *Journal of Physical Oceanography*, *41*, 586–600.

Bourgault, D., Kelley, D., & Galbraith, P. (2008). Turbulence and boluses on an internal beach. *Journal of Marine Research*, *66*, 563–588.

Bourgault, D., Kelley, D. E., & Galbraith, P. S. (2005). Interfacial solitary wave run-up in the St. Lawrence Estuary. *Journal of Marine Research*, *63*, 1551–1570.

Buijsman, M., McWilliams, J. C., & Jackson, C. (2010). East-west asymmetry in nonlinear internal waves from Luzon Strait. *Journal of Geophysical Research*, *115*, C10057. https://doi.org/10.1029/2009JC006004

Chang, M.-H., Lien, R.-C., Tang, T. Y., D'Asaro, E. A., & Yang, Y.-J. (2006). Energy flux of nonlinear internal waves in northern South China Sea. *Geophysical Research Letters*, *33*, L03607. https://doi.org/10.1029/2005GL025196

Chen, C., Hsu, J. R., Cheng, M., Chen, H., & Kuo, C. (2007). An investigation on internal solitary waves in a two-layer fluid: Propagation and reflection from steep slopes. *Ocean Engineering*, *34*, 171–184.

Cheriton, O., McPhee-Shaw, E. E., Shaw, W. J., Stanton, T. P., Bellingham, J. G., & Storlazzi, C. D. (2014). Suspended particulate layers and internal waves over the southern Monterey Bay continental shelf: An important control on shelf mud belts? *Journal of Geophysical Research: Oceans*, *119*, 428–444. https://doi.org/10.1002/2013JC009360

Connolly, T., & Kirincich, A. (2018). High-resolution observations of subsurface fronts and alongshore bottom temperature variability over the inner shelf. *Journal of Geophysical Research: Oceans*, *124*, 593–614. https://doi.org/10.1029/2018JC014454

Davis, K. A., & Monismith, S. G. (2011). The modification of bottom boundary layer turbulence and mixing by internal waves shoaling on a barrier reef. *Journal of Physical Oceanography*, *41*(11), 2223–2241.

DeCarlo, T. M., Cohen, A. L., Wong, G. T., Shiah, F. K., Lentz, S. J., Davis, K. A., et al. (2017). Community production modulates coral reef pH and the sensitivity of ecosystem calcification to ocean acidification. *Journal of Geophysical Research: Oceans*, *122*, 745–761. https://doi.org/10.1002/2016JC012326

DeCarlo, T. M., Karnauskas, K. B., Davis, K. A., & Wong, G. T. (2015). Climate modulates internal wave activity in the northern South China Sea. *Geophysical Research Letters*, *42*, 831–838. https://doi.org/10.1002/2014GL062522

Diamesses, P. J., & Redekopp, L. G. (2006). Numerical investigation of solitary internal wave-induced global instability in shallow water benthic boundary layers. *Journal of Physical Oceanography*, *36*, 784–812.

Diebels, S., Schuster, B., & Hutter, K. (1994). Nonlinear internal waves over variable topography. *Geophysical and Astrophysical Fluid Dynamics*, *76*(1–4), 165–192.

Duda, T. F., Lynch, J. F., Irish, J. D., Beardsley, R. C., Ramp, S. R., Chiu, C.-S., et al. (2004). Internal tide and nonlinear internal wave behavior at the continental slope in the northern South China Sea. *IEEE Journal of Oceanic Engineering*, *29*(4), 1105–1130.

Dunphy, M., Subich, C., & Stastna, M. (2011). Spectral methods for internal waves: Indistinguishable density profiles and double-humped solitary waves. *Nonlinear Processes in Geophysics*, *18*(3), 351–358.

Egbert, G. D., & Erofeeva, S. Y. (2002). Efficient inverse modeling of barotropic ocean tides. *Journal of Atmospheric and Oceanic Technology*, *19*(2), 183–204.

Emery, K. O., & Gunnerson, C. G. (1973). Internal swash and surf. *Proceedings of the National Academy of Sciences of the United States of America*, *70*(8), 2379–2380. https://doi.org/10.1073/pnas.70.8.2379

Fringer, O., Gerritsen, M., & Street, R. (2006). An unstructured-grid, finite-volume, nonhydrostatic, parallel coastal ocean simulator. *Ocean Model Online*, *14*(3–4), 139–173.

Fu, K., Wang, Y. H., Laurent, L. S., Simmons, H., & Wang, D. P. (2012). Shoaling of large-amplitude nonlinear internal waves at Dongsha Atoll in the northern South China Sea. *Continental Shelf Research*, *37*, 1–7.

Garrett, C., & Munk, W. (1979). Internal waves in the ocean. *Annual Review of Fluid Mechanics*, *11*, 339–369.

Green, R., Jones, N., Rayson, M., Lowe, R., Bluteau, C., & Ivey, G. (2018). Nutrient fluxes into an isolated coral reef atoll by tidally driven internal bores. *Limnology and Oceanography*.

Guo, C., & Chen, X. (2014). A review of internal solitary wave dynamics in the northern South China Sea. *Progress in Oceanography*, *121*, 7–23.

Hall, R. A., Huthnance, J. M., & Williams, R. G. (2013). Internal wave reflection on shelf slopes with depth-varying stratification. *Journal of Physical Oceanography*, *43*(2), 248–258.

Hausner, M., Suárez, F., Glander, K. E., Giesen, N. V. D., Selker, J. S., & Tyler, S. W. (2011). Calibrating single-ended fiber-optic Raman spectra distributed temperature sensing data. *Sensors*, *11*(11), 10,859–10,879.

Helfrich, K. R. (1992). Internal solitary wave breaking and run-up on a uniform slope. *Journal of Fluid Mechanics*, *243*, 133–154.

Helfrich, K. R., & Melville, W. K. (2006). Long nonlinear internal waves. *Annual Review of Fluid Mechanics*, *38*, 395–425.

Helfrich, K. R., & White, B. L. (2010). A model for large-amplitude internal solitary waves with trapped cores. *Nonlinear Processes in Geophysics*, *17*(4), 303–318.

Henderson, S. (2016). Upslope internal-wave Stokes drift, and compensating downslope Eulerian mean currents, observed above a lakebed. *Journal of Physical Oceanography*, *46*(6), 1947–1961.

Henyey, F. S., & Hoering, A. (1997). Energetics of borelike internal waves. *Journal of Geophysical Research*, *102*(C2), 3323–3330.

Hilgersom, K., van de Giesen, N. C., de Louw, P. G. B., & Zijlema, M. (2016). Three-dimensional dense distributed temperature sensing for measuring layered thermohaline systems. *Water Resources Research*, *52*, 6656–6670. https://doi.org/10.1002/2016WR019119

Hofmann, G. E., Smith, J. E., Johnson, K. S., Send, U., Levin, L. A., Micheli, F., et al. (2011). High-frequency dynamics of ocean pH: A multi-ecosystem comparison. *PLoS ONE*, *6*(12), e28983. https://doi.org/10.1371/journal.pone.0028983

Hosegood, P., Bonnin, J., & van Haren, H. (2004). Solibore-induced sediment resuspension in the Faeroe-Shetland Channel. *Geophysical Research Letters*, *31*, L09301. https://doi.org/10.1029/2004GL019544

Hsu, M.-K., & Liu, A. K. (2000). Nonlinear internal waves in the South China Sea. *Can. J. Remote Sensing*, *26*, 72–81.

Iribarren, C., Nogales, C. M. (1949). Protection des ports/, PIANC.

Kang, D., & Fringer, O. (2012). Energetics of barotropic and baroclinic tides in the Monterey Bay area. *Journal of Physical Oceanography*, *42*(2), 272–290.

Klymak, J. M., & Moum, J. N. (2003). Internal solitary waves of elevation advancing on a shoaling shelf. *Geophysical Research Letters*, *30*(20), 2045. https://doi.org/10.1029/2003GL017706

Klymak, J. M., Pinkel, R., Liu, A. K., & David, L. (2006). Prototypical solitons in the South China Sea. *Geophysical Research Letters*, *33*, L11607.

Kobs, S., Holland, D. M., Zagorodnov, V., Stern, A., & Tyler, S. W. (2014). Novel monitoring of Antarctic ice shelf basal melting using a fiber-optic distributed temperature sensing mooring. *Geophysical Research Letters*, *41*, 6779–6786. https://doi.org/10.1002/2014GL061155

Kundu, P. K., & Cohen, I. M. (2002). *Fluid mechanics* (2nd ed., p. 730). San Diego: Academic press.

Lamb, K. G. (2014). Internal wave breaking and dissipation mechanisms on the continental slope/shelf. *Annual Review of Fluid Mechanics*, *46*, 231–254.

Lamb, K. G., & Nguyen, V. T. (2009). Calculating energy flux in internal solitary waves with an application to reflectance. *Journal of Physical Oceanography*, *33*(3), 559–580.

Leichter, J. J., Stewart, H. L., & Miller, S. L. (2003). Episodic nutrient transport to Florida coral reefs. *Limnology and Oceanography*, *48*(4), 1394–1407.

Leichter, J. J., Wing, S. R., Miller, S. L., & Denny, M. W. (1996). Pulsed delivery of subthermocline water to Conch Reef (Florida Keys) by internal tidal bores. *Limnology and Oceanography*, *41*(7), 1490–1501.

Li, Q., & Farmer, D. M. (2011). The generation and evolution of nonlinear internal waves in the deep basin of the South China Sea. *Journal of Physical Oceanography*, *41*(7), 1345–1363.

Li, Q., Wang, B., Chen, X., Chen, X., & Park, J.-H. (2016). Variability of nonlinear internal waves in the South China Sea affected by the Kuroshio and mesoscale eddies. *Journal of Geophysical Research: Oceans*, *121*, 2098–2118. https://doi.org/10.1002/2015JC011134

Lien, R., D'Asaro, E. A., Henyey, F., Chang, M. H., Tang, T. Y., & Yang, Y. J. (2012). Trapped core formation within a shoaling nonlinear internal wave. *Journal of Physical Oceanography*, *42*(4), 511–525.

Lien, R., Tang, T. Y., Chang, M. H., & D'Asaro, E. A. (2005). Energy of nonlinear internal wave in the South China Sea. *Geophysical Research Letters*, *32*, L05615. https://doi.org/10.1029/2004GL022012

Lucas, A., Franks, P. J., & Dupont, C. J. (2011). Horizontal internal tide fluxes support elevated phytoplankton productivity over the inner continental shelf. *Limnology and Oceanography: Fluids and Environments*, *1*(1), 56–74.

MacKinnon, J. A., & Gregg, M. C. (2003). Mixing on the late-summer New England shelf—Solibores, shear, and stratification. *Journal of Physical Oceanography*, *33*, 1476–1492.

Martini, K., Alford, M., Kunze, E., Kelly, S., & Nash, J. (2013). Internal bores and breaking internal tides on the Oregon continental slope. *Journal of Physical Oceanography*, *43*(1), 120–139.

McSweeney, J. M., Lerczak, J. A., Barth, J. A., Becherer, J., Colosi, J. A., MacKinnon, J. A., et al. (2020). Observations of shoaling nonlinear internal bores across the Central California inner shelf. *Journal of Physical Oceanography*, *50*, 111–132.

Michallet, H., & Ivey, G. N. (1999). Experiments on mixing due to internal solitary waves breaking on uniform slopes. *Journal of Geophysical Research*, *104*(C6), 13,467–413,477.

Morton, B., & Blackmore, G. (2001). South China Sea. *Marine Pollution Bulletin*, *42*(12), 1236–1263. https://doi.org/10.1016/s0025-326x(01)00240-5

Nakayama, K., & Imberger, J. (2010). Residual circulation due to internal waves shioaling on a slope. *Limnology and Oceanography*, *55*(3), 1009.

Nash, J. D., Alford, M. H., & Kunze, E. (2005). On estimating internal-wave energy fluxes in the ocean. *Journal of Atmospheric and Oceanic Technology*, *22*(10), 1551–1570. https://doi.org/10.1175/JTECH1784.1

Nash, J. D., Kelly, S. M., Shroyer, E. L., Moum, J. N., & Duda, T. F. (2012). The unpredictable nature of internal tides on continental shelves. *Journal of Physical Oceanography*, *42*, 1981–2000.

Omand, M., Leichter, J. J., Franks, P. J., Guza, R. T., Lucas, A. J., & Feddersen, F. (2011). Physical and biological processes underlying the sudden surface appearance of a red tide in the nearshore. *Limnology and Oceanography*, *56*(3), 787–801.

Orr, M., & Mignerey, P. C. (2003). Nonlinear internal waves in the South China Sea: Observation of the conversion of depression internal waves to elevation internal waves. *Journal of Geophysical Research*, *108*(C3), 3064. https://doi.org/10.1029/2001JC001163

Padman, L., & Erofeeva, S. (2004). A barotropic inverse tidal model for the Arctic Ocean. *Geophysical Research Letters*, *31*, L02303. https://doi.org/10.1029/2003GL019003

Parsons, T., Maita, Y., & C. Lalli I, I. (1984). *A manual of chemical and biological methods for seawater analysis* (Vol. 1, p. 73). Ox ford, UK: Pergamon Press.

Pineda, J. (1991). Predictable upwelling and the shoreward transport of planktonic larvae by internal tidal bores. *Science*, *253*, 548–551.

Pineda, J. (1999). Circulation and larval distribution in internal tidal bore warm front. *Limnology and Oceanography*, *44*(6), 1400–1414.

Ramp, S., Yang, Y. J., & Bahr, F. L. (2010). Characterizing the nonlinear internal wave climate in the northeastern South China Sea. *Nonlinear Processes in Geophysics*, *17*(5), 481–498.

Reid, E., DeCarlo, T., Cohen, A., Wong, G., Lentz, S., Safaie, A., et al. (2019). Internal wave influence the thermal and nutrient environment on a shallow coral reef. *Limnology and Oceanography*.

Rogers, A. (1999). Distributed optical-fibre sensing. *Measurement Science and Technology*, *10*(8), R75.

Schmidt, G. M., Wall, M., Taylor, M., Jantzen, C., & Richter, C. (2016). Large-amplitude internal waves sustain coral health during thermal stress. *Coral Reefs*, *35*(3), 869–881.

Scotti, A., Beardsley, R., & Butman, B. (2006). On the interpretation of energy and energy fluxes of nonlinear internal waves: An example from Massachusetts Bay. *Journal of Fluid Mechanics*, *561*, 103–112.

Scotti, A., Beardsley, R. C., & Butman, B. (2007). Generation and propagation of nonlinear internal waves in Massachusetts Bay. *Journal of Geophysical Research*, *112*, C10001. https://doi.org/10.1029/2007JC004313

Scotti, A., & Pineda, J. (2004). Observation of very large and steep internal waves of elevation near the Massachusetts coast. *Geophysical Research Letters*, *31*, L22307. https://doi.org/10.1029/2004GL021052

Selker, J., van de Giesen, N., Westhoff, M., Luxemburg, W., & Parlange, M. B. (2006). Fiber optics opens window on stream dynamics. *Geophysical Research Letters*, *33*, L24401. https://doi.org/10.1029/2006GL027979

Shroyer, E., Moum, J. N., & Nash, J. D. (2009). Observations of polarity reversal in shoaling nonlinear internal waves. *Journal of Physical Oceanography*, *39*(3), 691–701.

Simmons, H., Chang, M.-H., Chang, Y.-T., Chao, S.-Y., Fringer, O. B., Jackson, C. R., & Ko, D. B. (2011). Modeling and prediction of internal waves in the South China Sea. *Oceanography*, *24*(4), 88–99.

Sinnett, G., & Feddersen, F. (2014). The surf zone heat budget: The effect of wave heating. *Geophysical Research Letters*, *41*, 7217–7226. https://doi.org/10.1002/2014GL061398

Sinnett, G., Feddersen, F., Lucas, A. J., Pawlak, G., & Terrill, E. (2018). Observations of nonlinear internal wave run-up to the surfzone. *Journal of Physical Oceanography*, *48*(3), 531–554.

Song, J. (2011). *Biogeochemical processes of biogenic elements in China marginal seas*. New York: Springer Science & Business Media.

St. Laurent, L. (2008). Turbulent dissipation on the margins of the South China Sea. *Geophysical Research Letters*, *35*, L23615. https://doi.org/10.1029/2008GL035520

Stastna, M., & Lamb, K. G. (2002). Large fully nonlinear internal solitary waves: The effect of background current. *Physics of Fluids*, *14*(9), 2987–2999.

Stastna, M., & Lamb, K. G. (2008). Sediment resuspension mechanisms associated with internal waves in coastal waters. *Journal of Geophysical Research*, *113*, C10016. https://doi.org/10.1029/2007JC004711

Stokes, M., Leichter, J. J., Wing, S., & Frew, R. (2011). Temperature variability and algal isotopic heterogeneity on a Floridian coral reef. *Marine Ecology*, *32*(3), 364–379.

Suárez, F., J Dozier, Selker, J. S., Hausner, M. B., & Tyler, S. W. (2011). Heat transfer in the environment: Development and use of fiber-optic distributed temperature sensing, INTECH Open Access Publishehr.

Tkachenko, K. S., & Soong, K. (2017). Dongsha Atoll: A potential thermal refuge for reef-building corals in the South China Sea. *Marine Environmental Research*, *127*, 112–125. https://doi.org/10.1016/j.marenvres.2017.04.003

Turkington, B., Eydeland, A., & Wang, S. (1991). A computational method for solitary internal waves in a continuously stratified fluid. *Studies in Applied Mathematics*, *85*(2), 93–127.

Tyler, S., Selker, J. S., Hausner, M. B., Hatch, C. E., Torgersen, T., Thodal, C. E., & Schladow, S. G. (2009). Environmental temperature sensing using Raman spectra DTS fiber-optic methods. *Water Resources Research*, *45*, W00D23. https://doi.org/10.1029/2008WR007052

Umeyama, M., & Shintani, T. (2006). Transformation, attenuation, setup, and undertow of internal waves on a gentle slope. *Journal of Waterway, Port, Coastal, and Ocean Engineering*, *132*(6), 477–486.

van Emmerik, T., Rimmer, A., Lechinsky, Y., Wenker, K. J. R., Nussboim, S., & van de Giesen, N. C. (2013). Measuring heat balance residual at lake surface using distributed temperature sensing. *Limnology and Oceanography: Methods*, *11*, 79–90.

Venayagamoorthy, S. K., & Fringer, O. B. (2007). On the formation and propagation of nonlinear internal boluses across a shelf break. *Journal of Fluid Mechanics*, *577*, 137–159.

Vercauteren, N., Huwald, H., Bou-Zeid, E., Selker, J., Lemmin, U., Parlange, M., & Lunati, I. (2011). Evolution of superficial lake water temperature profile under diurnal radiative forcing. *Water Resources Research*, *47*, W09522. https://doi.org/10.1029/2011WR010529

Vitousek, S., & Fringer, O. B. (2011). Physical vs. numerical dispersion in nonhydrostatic ocean modeling. *Ocean Model Online*, *40*(1), 72–86.

Vlasenko, V., & Hutter, K. (2001). Generation of second mode solitary waves by the interaction of a first mode soliton with a sill. *Nonlinear Processes in Geophysics*, *8*(4/5), 223–239.

Vlasenko, V., & Hutter, K. (2002). Numerical experiments on the breaking of solitary internal wavesover a slope–shelf topography. *Journal of Physical Oceanography*, *32*(6), 1779–1793.

Wall, M., Putchim, L., Schmidt, G., Jantzen, C., Khokiattiwong, S., & Richter, C. (2015). Large-amplitude internal waves benefit corals during thermal stress. *Proceedings of the Royal Society of London B: Biological Sciences*, *282*(1799).

Walter, R., Reid, E., Davis, K., Armenta, K., Merhoff, K., & Nidzieko, N. (2017). Local diurnal wind-driven variability and upwelling in a small coastal embayment. *Journal of Geophysical Research: Oceans*, *122*, 955–972. https://doi.org/10.1002/2016JC012466

Walter, R., Squibb, M., Woodson, C., Koseff, J., & Monismith, S. (2014). Stratified turbulence in the nearshore coastal ocean: Dynamics and evolution in the presence of internal bores. *Journal of Geophysical Research: Oceans*, *119*, 8709–8730. https://doi.org/10.1002/2014JC010396

Walter, R., Woodson, C., Leary, P., & Monismith, S. (2014). Connecting wind-driven upwelling and offshore stratification to nearshore internal bores and oxygen variability. *Journal of Geophysical Research: Oceans*, *119*, 3517–3534. https://doi.org/10.1002/2014JC009998

Walter, R., Woodson, C. B., Arthur, R. S., Fringer, O. B., & Monismith, S. (2012). Nearshore internal bores and turbulent mixing in southern Monterey Bay. *Journal of Geophysical Research*, *117*, C07017. https://doi.org/10.1029/2012JC008115

Wang, Y., Dai, C. F., & Chen, Y. Y. (2007). Physical and ecological processes of internal waves on an isolated reef ecosystem in the South China Sea. *Geophysical Research Letters*, *34*, L18609. https://doi.org/10.1029/2007GL030658

Wessels, F., & Hutter, K. (1996). Interaction of internal waves with a topographic sill in a two-layered fluid. *Journal of Physical Oceanography*, *26*(1), 5–20.

Winant, C. D. (1974). Internal surges in coastal waters. *Journal of Geophysical Research*, *79*(30), 4523–4526.

Wolanski, E., & Pickard, G. L. (1983). Upwelling by internal tides and Kelvin waves at the continental shelf break on the Great Barrier Reef. *Austrailian Journal of Marine and Freshwater Research*, *34*, 65–80.

Wong, G., T.-L. Ku, H. Liu, and M. Mulholland (2015), The oceanography of the northern South China Sea Shelf-Sea (NoSoCS) and its adjacent waters—Overview and highlights, edited, Elsevier.

Zhang, Z., Fringer, O. B., & Ramp, S. R. (2011). Three-dimensional, nonhydrostatic numerical simulation of nonlinear internal wave generation and propagation in the South China Sea. *Journal of Geophysical Research*, *116*, C05022. https://doi.org/10.1029/2010JC006424

Zhao, Z., & Alford, M. H. (2006). Source and propagation of internal solitary waves in the northeastern South China Sea. *Journal of Geophysical Research*, *111*, C11012. https://doi.org/10.1029/2006JC003644

Zhao, Z., Liu, B., & Li, X. (2014). Internal solitary waves in the China seas observed using satellite remote-sensing techniques: A review and perspectives. *International Journal of Remote Sensing*, *35*(11–12), 3926–3946.